The comptonization parameter from simulations of single-frequency, single-dish, dual-beam, cm-wave observations of galaxy clusters and mitigating CMB confusion using the Planck sky survey

Bartosz Lew[1,*] and Boudewijn F. Roukema[1]

[1]*Toruń Centre for Astronomy, Faculty of Physics, Astronomy and Informatics, Grudziadzka 5, Nicolaus Copernicus University, ul. Gagarina 11, 87-100 Toruń, Poland*

(Dated: Oct 10, 2016)

Systematic effects in dual-beam, differential, radio observations of extended objects are discussed in the context of the One Centimeter Receiver Array (OCRA). We use simulated samples of Sunyaev–Zel'dovich (SZ) galaxy clusters at low ($z < 0.4$) and intermediate ($0.4 < z < 1.0$) redshifts to study the implications of operating at a single frequency (30 GHz) on the accuracy of extracting SZ flux densities and of reconstructing comptonization parameters with OCRA. We analyze dependences on cluster mass, redshift, observation strategy, and telescope pointing accuracy. Using *Planck* data to make primary cosmic microwave background (CMB) templates, we test the feasibility of mitigating CMB confusion effects in observations of SZ profiles at angular scales larger than the separation of the receiver beams.

Keywords: Sunyaev-Zeldovich effect – cosmological simulations – galaxy clusters – radio surveys – methods: observational

arXiv:1608.03578v3 [astro-ph.IM] 18 Nov 2016

I. INTRODUCTION

Over the past several years many dedicated experiments have been used to detect the Sunyaev–Zel'dovich (SZ) effect (Sunyaev & Zeldovich 1970) from galaxy clusters at radio wavelengths [e.g., Berkeley-Illinois-Maryland Association (BIMA) (Dawson et al. 2006); Combined Array for Research in Millimeter-wave Astronomy (CARMA) (Mantz et al. 2014; Muchovej et al. 2012); the South Pole Telescope (SPT) (Reichardt et al. 2013); the Néel IRAM KIDs Array (NIKA) (Adam et al. 2014); the Atacama Pathfinder EXperiment Sunyaev–Zel'dovich Instrument (APEX-SZ) (Bender et al. 2016; Dobbs et al. 2006); the Arcminute Microkelvin Imager (AMI) (Rumsey et al. 2016; Zwart et al. 2008); *Planck* Surveyor (Planck Collaboration et al. 2011); the Atacama Cosmology Telescope (ACT) (Hasselfield et al. 2013); Array for Microwave Background Anisotropy (AMiBA) (Lin et al. 2016)]. Within the next few years, new observational facilities will become operational and will search for galaxy clusters, complementing the galaxy cluster census across the Universe [e.g., New IRAM KID Array 2 (NIKA2) on the Institut de Radio Astronomie Millimetrique 30 m telescope (Calvo et al. 2016)].

The One Centimeter Receiver Array (OCRA) (Browne et al. 2000; Peel et al. 2011) is one of the experiments capable of detecting the SZ effect at 30 GHz using beam-switching radiometers installed on a 32-meter radio telescope (Lancaster et al. 2011, 2007). OCRA will be mostly sensitive to SZ clusters with virial size $> 3'$ and hence to clusters at redshifts in the range $0.1 < z < 0.5$ and with masses $M_{\rm vir} > 3 \times 10^{14} M_\odot/h$ (Lew et al. 2015). However, a single frequency, beam-switching system may suffer from confusion with the primordial cosmic microwave background (CMB) or suffer from systematic error when observing extended sources.

Confusion effects due to the CMB were investigated in detail by Melin et al. (2006) for AMI, SPT and *Planck* Surveyor. It was found that for single frequency instruments, such as AMI (a 15 GHz interferometer), the photometric accuracy that contributes to the accuracy of the reconstructed comptonization parameter is strongly limited due to primary CMB confusion.

In Lew et al. (2015) the impact of CMB flux density confusion at 30 GHz was investigated, in particular for the OCRA/RT32 (32 m Radio Telescope in Toruń, Poland) experiment. It was found that the 1σ thermal SZ (tSZ) flux density uncertainty due to CMB confusion should be of the order of 10% for the range of clusters detectable with OCRA. However, in that work, the impact on the reconstructed comptonization parameter in the presence of the CMB and radio sources was not calculated directly for the case of dual-beam differential observations.

The $\approx 3'$ separation of OCRA beams is very effective in CMB removal, but large correcting factors are required to compensate for the missing SZ signal (after accounting for point sources) (Lancaster et al. 2007). Thus, there is a trade-off between compromising photometry by the primary CMB signal versus losing flux due to the differential beam pattern. In between these extremes, there should exist an optimal separation of differential beams that would need to be defined by criteria that aim to maximize CMB removal and minimize SZ flux density removal.

In this paper, we reconsider the issue of systematic effects on the reconstructed comptonization parameter from single frequency, beam-switched observations performed with a cm wavelength radiometer. We consider a particular instrumental setting for the OCRA/RT32 experiment and an extension to the standard observation scheme that previously involved only the angular scales defined by the receiver feeds. The extension adds additional beam pointings that map cluster peripheries, further from the central core than the initial pointings.

The *kinetic* SZ (kSZ) may significantly modify the brightness of the cluster peripheries that are integrated with the reference beam. The significance of this effect depends on a combination of the peculiar velocities of the intra-cluster medium (ICM) and internal gas clumps, but at cm wavelengths, the kSZ only weakly modifies the central brightness.

With dual-beam observations, the reference beam background coverage improves while integrating along arcs around

*blew@astro.uni.torun.pl

the cluster center as the field of view (FOV) rotates. However, due to the small angular size of the arcs, the chance of zeroing the average background may be low, depending on the alignment with the CMB pattern. We investigate the significance of this effect depending on observational strategy.

For experiments limited by the size of the focal plane array the integration time required to generate a radio map and to probe the outer regions of a galaxy cluster is significant and can make the observation prohibitive. Therefore, previously, the method of reconstructing comptonization parameters from OCRA observations of cluster central regions required inclusion of X-ray luminosity data in order to find the best fitting β-model for each cluster, and correction for the SZ power lost due to the close beam separation. However, this approach relies on the cluster model assumptions and makes the radio SZ measurements dependent on X-ray measurements of the cluster. Another possible approach is to observe SZ clusters out to larger angular distances but retain averaging over a range of parallactic angles. This is done at the cost of incurring extra noise due to weak tSZ in cluster peripheries and stronger systematic effects due to CMB.

An OCRA-SZ observational program is presently underway. In support of this and similar efforts, we also investigate the possibility of mitigating CMB confusion by using the available *Planck* data. Finally, we calculate the astrometric pointing and tracking accuracy requirements needed to attain a given accuracy in flux density reconstruction.

In Section II we review the current observing strategy and discuss its possible extensions. In Section III we briefly outline our numerical simulation setting. Section III B describes the construction of CMB templates from the currently available *Planck* data. Section III C describes simulated samples of galaxy clusters used for the flux-density analyses. The main results are in Sec. IV. Final remarks and conclusions are in Sections V and VI respectively.

II. OBSERVATIONAL STRATEGY

The common position-switching mode of observing (Lancaster et al. 2011) is that in which the reference beam non-uniformly (due to varying FOV rotation speed) integrates the background along arcs $\approx 3'$ from the source. In Fig. 1 (*top-right* panel), circles denote OCRA beamwidths for a typical observational scheme (Birkinshaw & Lancaster 2005). First, the beam pair "A–B" measures the difference signal between the cluster center and periphery, respectively. The beam pair is then "switched", i.e. translated to configuration "C–A" with a swap of the roles of the primary and reference beams, so that beams "C" and "A" now trace the cluster periphery and center, respectively. The position switching cycle is closed by returning to the initial configuration "A–B" and the cycle is repeated.

As the Earth rotates, the reference beams sweep arcs around the cluster center and probe different off-center background regions (beam B becomes B' and C becomes C'). The beam position-switching reduces fluctuations due to atmospheric turbulence on time scales of a few tens of seconds. At shorter time scales fluctuations due to receiver-gain instability and atmospheric absorption are reduced by switching and differentiating signals in receiver arms by means of electronically-controlled phase switches (Lancaster et al. 2011; Peel 2010).[1]

An extension to this pattern can be realized by adding an extra beam pointing "D". In this case an observation cycle would be extended so that a beam pair would observe differences between "A–B", then "B–D" and followed by "A–B", again probing the cluster peripheries for varying parallactic angles. This scheme can be extended to both sides of the cluster and to larger distances from the cluster center. In Fig. 1 (*top-left* panel) the projected beamwidths of the OCRA-f receiver focal plane are shown (black circles) overlaid on a nearby galaxy cluster seen through the SZ effect. The extra beam pointing "D" for the whole array is shown with blue circles. In the following sections we investigate the implications of such an extended observation scheme using numerical simulations.

III. SIMULATIONS

A. LSS and SZ effect

For the main results in this work we use the simulation approach described in Lew et al. (2015), with a few modifications. In particular, for the same field of view ($\approx 5.2^\circ$) we use an increased map resolution of $\approx 0.9''$. In observational practise, often only the central comptonization parameter value is quoted, so we include the kSZ signal calculated as a contribution to the measured Compton y-parameter for the appropriate frequency.

In this analysis we neglect the large-scale foreground galactic synchrotron, free–free and dust emissions. We assume these to be smooth enough to be removed in differential observations.

We assume that atmospheric effects and receiver noise are mitigated by sufficiently long integrations (see Sect. II and Birkinshaw & Lancaster (2005)). Systematic errors in flux density estimation that we neglect include feed and elevation dependent beam response, feed and elevation dependent sidelobes, and elevation dependent antenna gain. We defer treatment of these effects to a separate analysis of end-to-end full OCRA focal plane simulations. Although the simulated maps include some of the effects of halo–halo LOS projections, the significance of the projection effects on the y-parameter photometry are not the main focus of the present study. These effects should be small in this study, since we only consider the most massive systems at the FOV generation stage.

A cluster is not necessarily observed at the position that maximises the SZ signal. For an X-ray selected galaxy cluster, SZ observations can be centered at the maximum of the X-ray signal, but this may have a small offset with respect to the maximum of the SZ signal, although the difference should be rather

[1] Beam switching is realized at the rate of 277 Hz which improves the $1/f$ knee of the resulting difference signal power spectrum roughly by an order of magnitude; typically down to frequencies $0.1\mathrm{Hz} < f_{\mathrm{knee}} < 1\mathrm{Hz}$.

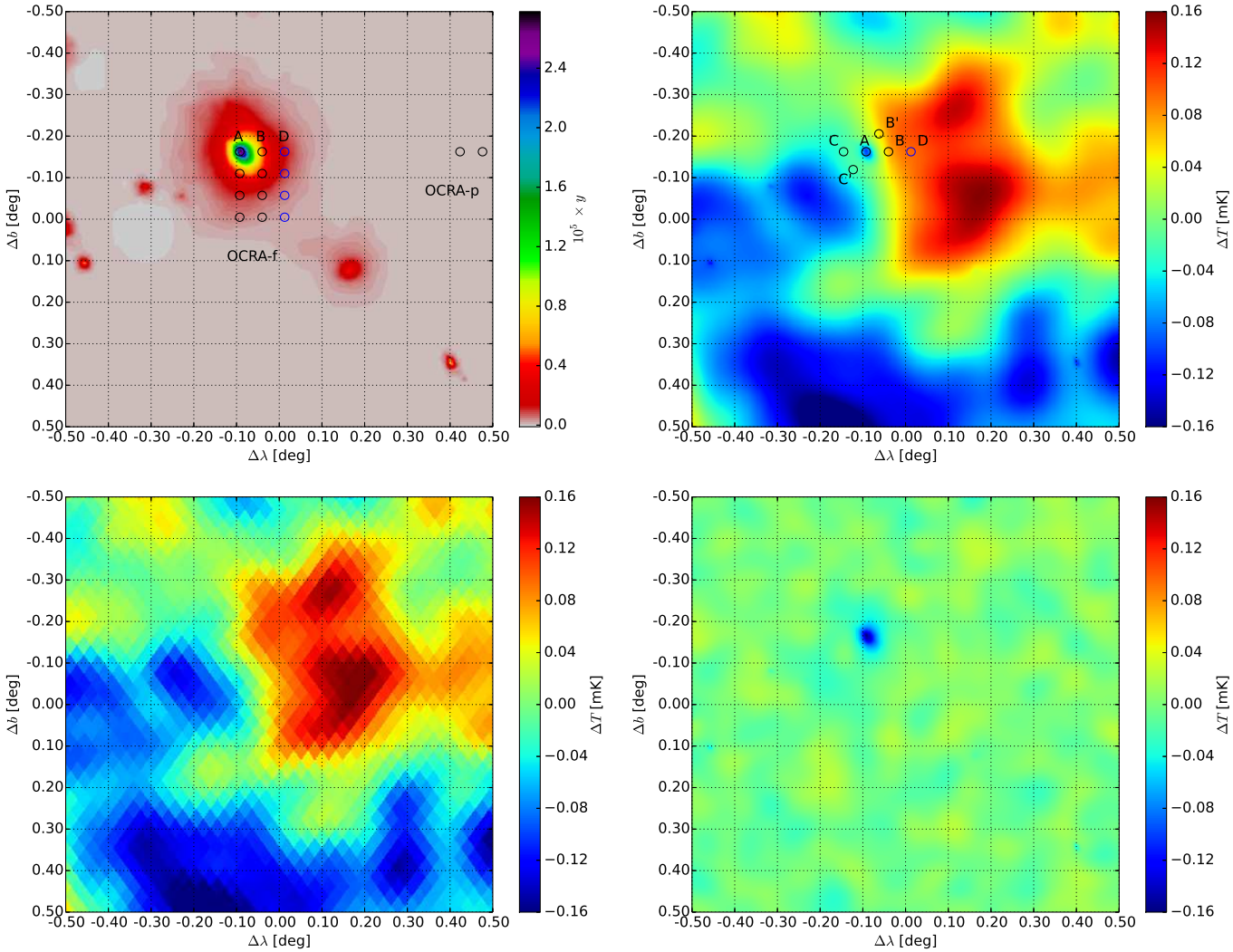

Figure 1: (*Top-left*) Projected map of the the line-of-sight (LOS) integrated comptonization parameter for a selected halo, and (*top-right*) simulated CMB temperature fluctuations ΔT including both primary CMB as well as tSZ and kSZ effects induced by the halo. (*Bottom-left*) 217 GHz *Planck* resolution simulation – the Gaussian CMB ΔT signal smoothed with a half-power beam width (HPBW) of $\approx 5'$ and including a realistic *Planck* noise realization (see Sec. III B). This map is used to make a high resolution CMB template by means of a smooth-particle interpolation. (*Bottom-right*) Residual map: primary CMB including tSZ minus interpolated *Planck* simulation (Sec. III B). The variance of the residual map (without SZ effects) is about one order of magnitude smaller than that measured using maps that include CMB. In the *top-right* panel the circles denote OCRA beamwidths traversing over the background CMB for a typical observational scheme (see Sec. II for details). In the *top-left* panel black circles represent the full focal plane of OCRA receivers.

small. This will effectively translate into pointing errors that we model in this work.

The OCRA beam separation is $s_{\rm OCRA} = 0.0526 \pm 0.0010^\circ$ (Fig. 1), which we adopt in this work. Within the measurement accuracy this does not depend on sky direction.

B. CMB templates

The *Planck* mission has provided full sky maps of the CMB temperature fluctuations at several frequencies, including 217 GHz, where the tSZ signal is minimal. This opens up the possibility to correct the differential SZ observations at other frequencies by removing a customized CMB template and thus reduce the CMB confusion in single frequency observations, provided that: (i) the small scale noise level of the template is low, (ii) the angular resolution of the data is sufficient and (iii) diffuse Galactic foregrounds can be neglected. In practise, requirement (iii) may exclude all or most of the sky regions covered by *Planck* frequency maps on either side of the Galactic Plane.

In order to test the usefulness of *Planck* data in minimizing the CMB-induced variance in the measured flux densities with a single-frequency instrument, we generate CMB simulations for *Planck*'s 217 GHz frequency band using simulated CMB power spectrum (Lewis et al. 2000) and assuming cos-

mological parameters as in Lew et al. (2015). We assume a Gaussian beam transfer function defined by a full-width half maximum FWHM = $5.02'$ (Planck Collaboration et al. 2016b) and use realistic and publicly available 217 GHz *Planck* receiver noise simulations[2] at Healpix (Górski et al. 2005) resolution $n_s = 2048$.

We simulate the primary CMB up to $\ell_{\rm max} = 3500$,[3] i.e. the OCRA beam separation. In order to create the final CMB template with $\approx 0.9''$ resolution in small FOVs, we use a smooth-particle interpolation of the projected field (as discussed in Lew et al. 2015).

Real observations at 217 GHz will contain kSZ contributions, which we ignore for generation of simulated templates. For each realization of the simulated template, we store maps with CMB signal, and maps with the CMB smoothed with the instrumental beam and contributed by a *Planck* noise realization (Fig. 1). The former is used for simulating astrophysical signals (SZ) in FOVs, while the latter is used for removing a *Planck*-compatible version of CMB contamination, for the same FOVs. Each FOV simulation is made at fixed galactic latitude $b = 40°$, but at a different galactic longitudes to account for variations due to direction dependent properties of *Planck* noise.

The single frequency maps from *Planck* mission are contaminated by foregrounds other than the cluster tSZ and kSZ signals, especially at low galactic latitudes. Since in the current work we do not investigate galactic foregrounds we additionally analyze another set of simulations based on the foreground-reduced map generated with the needlets-based internal linear combination (NILC) algorithm (Planck Collaboration et al. 2016a). The algorithm (Delabrouille et al. 2009) provides a very clean primary CMB map outside of masked regions which mask Galactic Plane and bright point sources (together $\approx 3.6\%$ of the full sky). We simulate the NILC map using the published beam transfer function, and use the full mission NILC rendition of ringhalf-1 and ringhalf-2 half difference maps to generate a *Planck* NILC-compatible noise realization. We verified that the resulting NILC simulations are compatible with the *Planck* NILC map in terms of their angular pseudo-power spectra. Slight differences in the high-ℓ regime of up to a few percent are present due to our choice of cosmological parameter values that is consistent with the WMAP9 results.

The NILC map resolution simulations are similar to those of the 217 GHz map, so in Fig. 1 we only show the map for the 217 GHz case.

C. Simulated galaxy cluster samples

For the analyses presented in Sect. IV, we construct two galaxy cluster samples. The first one, hereafter referred as *"targeted"* (Fig. 2 thick solid lines) is constructed by selecting the heaviest halos [$M_{\rm vir} > 4\times10^{14}M_\odot/h$ (see Table I)], from each independent simulation volume and using each recorded simulation snapshot. We impose a low redshift cut-off $z > z_{\rm min}$ to remove very extended clusters. The choice of redshifts for which simulation snapshots are taken is made such that the simulation volume continuously fills comoving space out to the maximal redshift (see Fig.1 of Lew et al. (2015)). For each simulation volume we apply random periodic coordinate shifts of the particles within, and we apply random coordinate switches. This (i) improves redshift space coverage and (ii) yields cluster SZ surface brightness profiles in different projections, at the cost of generating a partially correlated sample.

The second sample, hereafter referred to as *"blind"* (Fig. 2 thin solid lines), is generated using a blind survey approach (as in Lew et al. (2015)). We generate 37 FOV realizations each $\approx 27\,{\rm deg}^2$ together covering a sky area of $\approx 1000\,{\rm deg}^2$. From each realization we select halos with virial masses $M_{\rm vir,c} > 2\times10^{14}M_\odot/h$.

The solid angle integrated comptonization for any given halo ($Y = \int y(\hat{\mathbf{n}})d\Omega$) depends on a combination of halo redshift and mass. The *"blind"* sample is dominated by lighter halos than those found in the SPT sample (Fig. 2), although redshift space

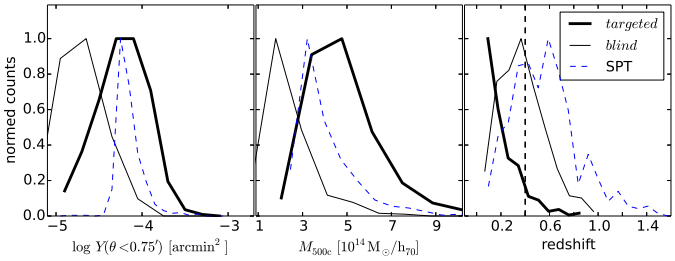

Figure 2: Distribution of the solid-angle–integrated comptonization parameter Y integrated within the angular radius $\theta < 0.75'$ from the cluster center (*left*); distribution of cluster total mass measured within a volume with mean mass density 500 times higher than the critical density of the Universe at the cluster's redshift (*middle*); and distribution of redshifts (*right*) for the simulated cluster samples (solid lines) and for the SPT cluster sample (Bleem et al. 2015) (dashed lines). For each simulated sample only halos with $M_{\rm vir} > M_{\rm vir,min}$ and $z > z_{\rm min}$ are chosen (see Table I). The vertical dashed line shows the division into high-z and low-z sub-samples that is used later in the analysis.

Table I: Selection criteria used for constructing galaxy cluster samples.

Parameter	Sample/Value	
	"targeted"	*"blind"*
$z_{\rm min}$	0.05	0.0
$M_{\rm vir,min}\,[10^{14}M_\odot/h]$	4.0	2.0
halo selection	full simulation volume	$5.2°\times5.2°$ FOV
halo count[a]	475	361
Sub-samples		
low-$z \le 0.4$	426	214
high-$z > 0.4$	49	147

[a] The actual number of halos used in statistical analyses are slightly different as they are further screened for halos that lie well within the projected FOV, which is required for simulating dual-beam observations at all possible parallactic angles and beam separations in a consistent way.

[2] `http://pla.esac.esa.int/pla/#maps`

[3] The variance lost due to neglecting even higher multipoles is negligibly small ($\lesssim 0.004\%$) and well below the cosmic variance uncertainty.

distributions of the two are similar. Hence, the bulk of the *"blind"* sample halos yields lower $Y(\theta < 0.75')$ values than those in the SPT sample (Fig. 2). Although increasing the lowest mass limit for the halos of the *"blind"* sample tends to make its mass and redshift distributions more consistent with those of the SPT sample, it reduces the numbers of halos, thus increasing Poisson noise. For the statistical analysis in this work, larger simulations and more FOV realizations than are currently available would be required to reach consistency. Therefore, we use this sample for tSZ analyses of simulated dual beam observations, bearing in mind that in this limit of weak SZ effects, CMB confusion is expected to be the most significant. On the other hand, the *"targeted"* sample is expected to be less affected by CMB confusion.

In order to investigate the differences between compact and extended SZ clusters we further split our cluster samples by redshift at $z = 0.4$ (Table I). This split roughly corresponds to half of the radial comoving distance to $z = 1.0$, beyond which we do not observe any heavy (Fig. 2) halos in our simulations. We find that the low-z and high-z samples mainly differ due to the strength of the SZ effects, and due to the presence of substructures, being respectively stronger and more abundant in the low-z subset. Examples for halos from low-z and high-z samples are shown below in Fig. 7.

IV. ANALYSIS AND RESULTS

A. Systematic effects from beam separation

Dual beam difference observations capture only a fraction of the intrinsic flux density, depending on the physical extent of the source, its redshift and the angular separation of the beams. We define this fraction as

$$F(\theta_b, s, q_{\rm max}) = \left\langle \frac{S_0^{\rm x}(\theta_b, s) - S_r^{\rm x}(\theta_b, s, \hat{\mathbf{n}}_{\mathbf{i}})}{S_0^{\rm tSZ}(\theta_b)} \right\rangle_i , \qquad (1)$$

where $S_0^{\rm x}$ is the measured central flux density per beam induced by effect "x", e.g. x = tSZ, $S_0^{\rm tSZ}$ is the true central flux density per beam due to tSZ (neglecting CMB, point sources, and other effects), $S_{\rm r}^{\rm x}$ is the flux density per beam due to effect "x" in the reference beam direction ($\hat{\mathbf{n}}_i$), θ_b is the instrumental half-power beam width (HPBW), and s is the angular separation of the beams. $N_{\rm r} = 500$ reference beam directions ($\hat{\mathbf{n}}_i$) are chosen randomly from a uniform distribution of parallactic angles ($q \in [0, q_{\rm max}]$), where the upper limit $q_{\rm max}$ is a free parameter.

For each halo, we measure these fractions F by integrating specific intensity directly from high resolution maps, and using the mean over the $N_{\rm r}$ values of q. If there is no CMB contamination, i.e. setting x = tSZ, so that $S_0^{\rm x} = S_0^{\rm tSZ}$ and $S_{\rm r}^{\rm x} = S_{\rm r}^{\rm tSZ}$, then $F \leq 1$ and $1 - F$ represents the fraction of the signal lost only due to the closeness of the beam angular separation.

The impact of beam separation on the dual-beam observations is shown in Figs. 3 and 4 for the *"blind"* and *"targeted"* samples respectively, for an idealistic case of exact pointing—i.e., no pointing inaccuracies are allowed ($\epsilon_p = 0$). In these figures, the median F (from all halos matching the selection criteria) is plotted along with a 68% confidence region. Clearly, dual-beam observations at larger beam separations are less biased than observations at smaller beam separations, and the 68% confidence range generally shrinks as s increases.

The significance of the primary CMB fluctuations for the dual-beam observations is estimated by setting x = tSZ+CMB, i.e., $S_0^{\rm x} = S_0^{\rm tSZ+CMB}$, $S_{\rm r}^{\rm x} = S_{\rm r}^{\rm tSZ+CMB}$. While the median F does not differ significantly from the pure tSZ case, the 68% confidence region significantly increases with beam separations due to primary CMB confusion. For example, since a primordial CMB fluctuation has a good chance of being of the same sign as the SZ signal at the cluster center but of the opposite sign in a distant reference beam, F can easily be greater than unity, as is clear in Fig. 3. As expected, the increase is stronger in the *"blind"* sample/high-z sub-sample than in the *"targeted"* sample/low-z sub-sample, due to differences in amplitudes of SZ effects compared to the level of CMB fluctuations.

Comparing Figs. 3 and 4 it is clear that the main difference is the relative significance of the CMB as a source of confusion and the amount of residual biasing. However, for any individual high-z and/or low-mass cluster observation, the measured flux density can be biased substantially. This can be inferred from the size of the 1σ tSZ+CMB confidence region. Even observations of the most massive clusters, which are the least affected by the presence of the CMB, can be biased substantially depending on the angular scales being measured (s) (Fig. 4 left panels). In the figure, the trade-off between CMB confusion due to observations at larger angular scales and the level of biasing (F) in the limit of small s is clearly seen.

For clusters that are small relative to the beam size, measurements far away from the cluster center are not really needed as the F values approach unity relatively fast (e.g. *"blind"* / high-z sample in Fig. 3). At the OCRA beam separation (the vertical line in the figures) the primary CMB does not strongly contribute to the scatter in flux density measurements. This is even more so in the case of the *"targeted"* sample of heavy and low-z clusters. On the other hand, the most massive halos (Fig. 4) require significant ($> 10\%$) flux density corrections even at large beam separations (although these may partially be generated by projection effects discussed in Sec. V).

It is clear that in the two cluster samples, kSZ only slightly increases the scatter in F at the OCRA beam separation, as expected at 30 GHz.

The impact of *Planck* based CMB template removal is shown in green. The calculation is done by setting x = tSZ+CMB−template in Eq. 1, i.e., $S_0^{\rm x} = S_0^{\rm tSZ+CMB-template}$, $S_{\rm r}^{\rm x} = S_{\rm r}^{\rm tSZ+CMB-template}$. From Figs. 3 and 4 it is clear that at the OCRA beam separation, and for the full range of parallactic angles, the *Planck* template does not significantly help, or does not help at all, in reducing the confusion due to primary CMB. However, in observations that probe larger angular separations, the CMB template removal can substantially reduce the 1σ contours. The template removal may also be useful for observations of high-z massive clusters for which mapping larger angular distances away from the central directions still appears to be well motivated. Both in the high-z and low-z sub-samples of the *"targeted"* sample the template reduces the tSZ+CMB scatter nearly down to the level limited by the intrinsic tSZ scat-

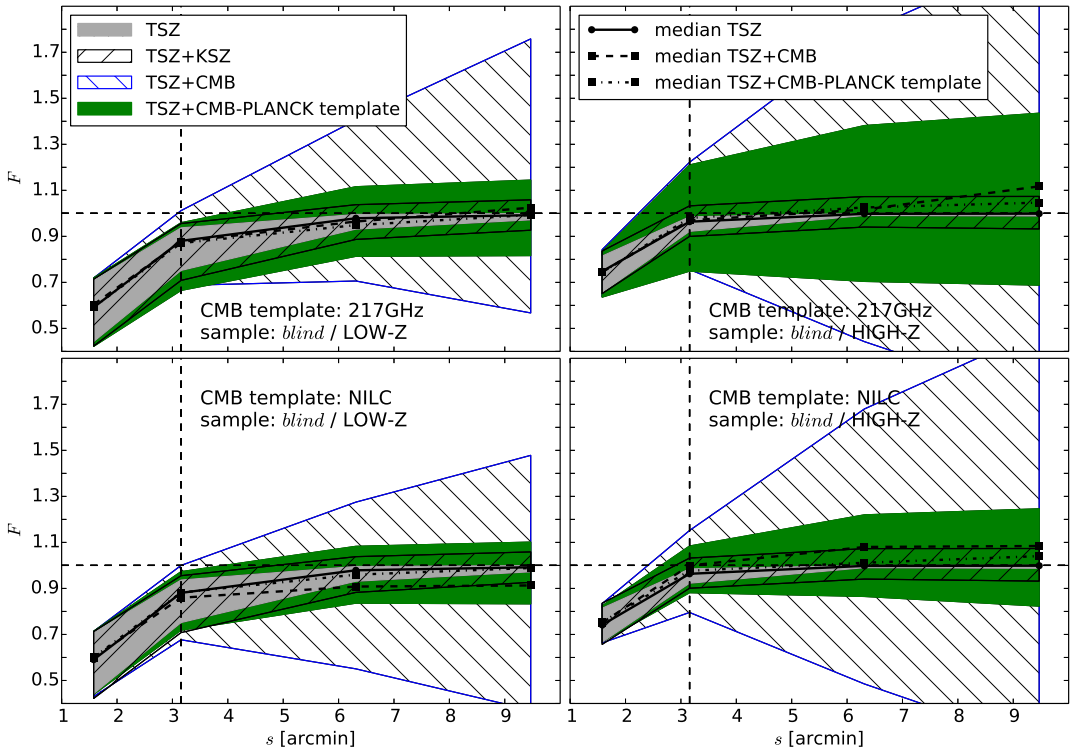

Figure 3: Simulated fractions (F) of SZ effect flux density at 30 GHz recovered from difference, dual beam observations of clusters from *"blind"* sample as a function of beam angular separation s and redshift range. The shaded/hatched regions map the 68% confidence regions (CR) in the distribution of F. The scatter in F calculated from maps containing only tSZ signal is shown in gray. The backslash-hatched region shows the effects of primary CMB on biasing the tSZ flux density measurements. The forward-slash–hatched region shows the intrinsic scatter due to kSZ when converted and embedded into the 30 GHz thermal SZ effect maps. The green region shows the improvements in decreasing the intrinsic scatter in F as a result of subtracting the Planck CMB template from CMB+tSZ simulated maps prior to flux density calculations. The median F values are shown as lines. The 68% confidence regions about the medians become asymmetric as the beam separation increases (simulation sample error also becomes obvious in the TSZ+CMB case by comparing upper to lower plots; the TSZ, TSZ+KSZ, and TSZ+CMB cases are statistically equivalent between the upper and lower panels). The vertical dashed line marks the actual separation of OCRA beams fixed by the telescope optics. It is assumed that the reference beam covers an annulus around a galaxy cluster within parallactic angle range $[0^\circ, 180^\circ]$ on either side of the central direction, and that pointing error $\epsilon_p = 0$ (see Sec. IV F).

ter for the full range of s studied here (Fig. 4).

B. Parallactic angle dependence

In practise, the OCRA observations exploit beam and position switching (Sect. II) but it is unrealistic to cover the full parallactic angle range: i.e. $q \in [0^\circ, q_{\rm max}]$ where $q_{\rm max} = 360^\circ$.

It was already known that position switching (Birkinshaw & Lancaster 2005) significantly mitigates atmospheric instabilities over the time scale of tens of seconds by (i) subtracting linear drifts caused by large-scale precipitable water vapor (PWV) fluctuations (Lew & Uscka-Kowalkowska 2016), (ii) accounting for beam response asymmetries, and (iii) maximizing the probability of avoiding (masking out) intervening radio sources that can significantly bias the SZ measurement. In this section, we show that position switching is also efficient in mitigating the confusion due to primordial CMB, even with a very modest coverage of parallactic angles.

There should not be any statistical correlation between primordial CMB fluctuations and the locations of heavy halos. Moreover, galaxy clusters have small angular sizes compared those representing most of the CMB power. Thus, clusters should mostly lie on slopes rather than peaks or troughs in the CMB map. Hence, sampling SZ flux density differences at opposite sides of a galaxy cluster core should help average out the primordial CMB in comparison to one-sided observations. We confirm that this is indeed the case and find that this improvement is reached at even moderate values of $q_{\rm max}$.

We calculate $F(s)$ [Eq. (1)] for maps containing tSZ and CMB using mean flux density estimates either according to the position switching observation scheme or without it. As before, each measurement is an average of 500 dual-beam pointings at different q but drawn randomly from within the range $[0^\circ, q_{\rm max}]$ where $q_{\rm max} \in \{180^\circ, 90^\circ, 45^\circ, 22.5^\circ\}$.

The result is shown in Fig. 5 for $q_{\rm max} = 22.5^\circ$. By comparing the left panel of this figure with the top-left panel of Fig. 3 it is clear that even strongly incomplete coverage of the parallactic angles does not cause significant broadening of the 68% confidence level (CL) contours. However, when position switching

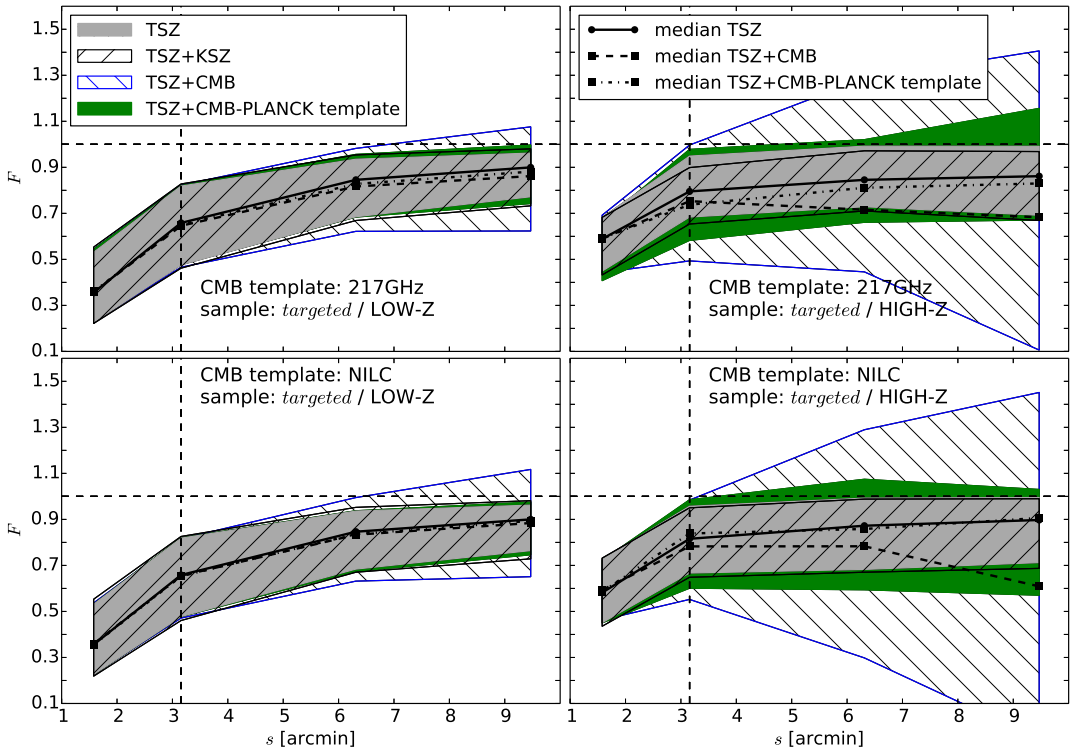

Figure 4: As in Fig. 3 but for the *"targeted"* sample.

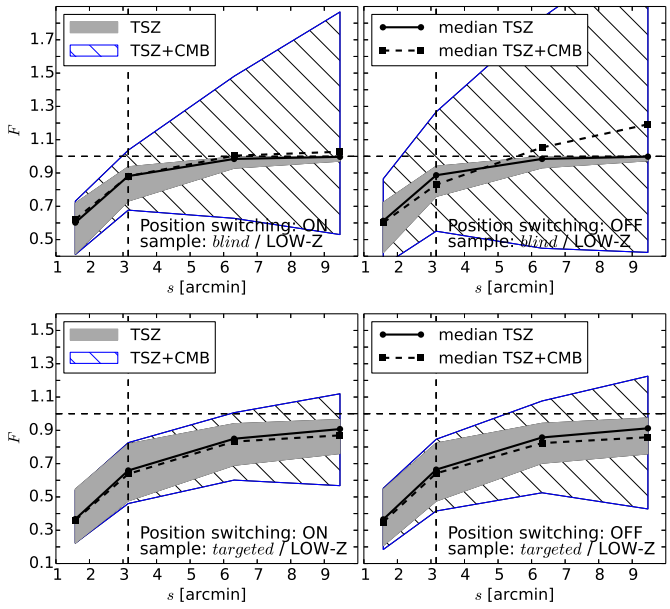

Figure 5: As in Figs 3 and 4, but for observations where the reference beam covers an annulus around a galaxy cluster within parallactic angle range $[0^\circ, 22.5^\circ]$ on either side of the cluster direction (left), or only on one side of the cluster direction (right) for the *"blind"* (top) and *"targeted"* (bottom) samples.

is not used (right panels in Fig. 5), the confusion due to primordial CMB is stronger. As before, the *"targeted"* sample of the heaviest halos is less affected by the presence of the CMB, but the effect of not using position switching is still visible, even at $s = s_{\rm OCRA}$ (vertical line in Fig. 5, bottom panels).

C. Systematic effects in redshift space

The F factor depends on a cluster's angular size, which in turn depends on the cluster's redshift. We model the dependence of $F(\theta_b, s, p)$ (Eq. 1) on redshift by defining:

$$F_{\rm m}(\theta_b, s, \beta, \theta_c) = 1 - \frac{\int b(\hat{\mathbf{n}}, \theta_b, s)\, I_{\rm SZ}(\hat{\mathbf{n}}, \beta, \theta_c)\, {\rm d}\Omega}{\int b(\hat{\mathbf{n}}, \theta_b, s=0)\, I_{\rm SZ}(\hat{\mathbf{n}}, \beta, \theta_c)\, {\rm d}\Omega}, \quad (2)$$

where $b(\hat{\mathbf{n}}, \theta_b, s)$ is a Gaussian beam profile with beam width θ_b , offset by angular distance s from the cluster center direction $\hat{\mathbf{n}}_\mathbf{0}$. We choose $s = s_{\rm OCRA}$ to simulate the position of the OCRA reference beam when the primary beam points at the cluster center. $I_{\rm SZ}(\hat{\mathbf{n}}, \beta, \theta_c)$ is a normalized, LOS integrated β profile that represents the SZ effect surface brightness:

$$I_{\rm SZ}(\hat{\mathbf{n}}, \beta, \theta_c) \propto \left(1 + \frac{\theta^2}{\theta_c^2}\right)^{\frac{1}{2} - \frac{3}{2}\beta}, \quad (3)$$

where $\theta_c = 2r_c/d_A(z)$ is the angular diameter of the observed galaxy cluster defined in terms of its core size r_c, θ is the angle from $\hat{\mathbf{n}}$ to $\hat{\mathbf{n}}_\mathbf{0}$, and $d_A(z)$ is the angular diameter distance. $F_{\rm m}$ depends on the choice of cosmological parameters and on

Table II: Parameters of halos selected from Fig. 6. The parameter y_0 is the maximal value of the LOS integrated comptonization parameter.

ID	z	F	$M_{\rm vir}$ $[10^{14}M_\odot/h]$	$y_0 \times 10^5$	comment[a]
"targeted" sample (rect. "1" selection)					
1	0.552	0.39	4.6	1.38	P
2	0.520	0.43	4.7	3.40	P
3	0.885	0.49	4.4	0.71	P, D
4	0.429	0.47	4.6	2.10	P, E
5	0.366	0.44	5.1	1.75	P
6	0.370	0.53	4.9	2.10	P
7	0.349	0.50	5.1	3.10	P
8	0.337	0.34	5.4	3.70	P
9	0.388	0.50	4.4	2.2	P
"targeted" sample ($M_{\rm vir} > 12.7 \times 10^{14}M_\odot/h$)					
10	0.103	0.41	13.8	11.2	D
11	0.109	0.56	14.6	25.6	R, P
12	0.193	0.49	12.8	5.6	E, D, S, P
"blind" sample (rect. "1" selection)					
13	0.367	0.44	2.1	0.93	P
"targeted" sample (rect. "2" selection)					
14	0.182	0.64	11.3	6.68	D
15	0.268	0.77	12.6	9.50	D
16	0.169	0.75	10.1	10.3	R, S

[a] P - reference beam flux density contamination from another halo due to LOS projection; D - disturbed morphology; E - elongated shape; R - regular morphology (virialized halo); S - sub-halo(s) present;

the chosen cluster density profile. We calculate $F_{\rm m}$ for ΛCDM cosmological parameters: $h = 0.7$, $\Omega_m = 0.3$, $\Omega_\Lambda = 0.7$, and for an Einstein–de Sitter cosmological model. For our redshift range we find that the dependence on cosmological parameters is weak compared to the dependence on the halo density profile (Fig. 6). We also calculate $F_{\rm m}$ for the case of a Gaussian halo but find that such profile is strongly disfavored by simulations as $F_{\rm m}$ approaches unity at fairly low redshifts.

The simplest β-model does not allow for the steepening of density profiles with increasing θ. However, X-ray observations suggest that such steepening is real (e.g. Vikhlinin et al. 2006), and it is expected that at large distances from cluster cores (or higher redshifts) the β-model yields lower $F_{\rm m}(z)$ values than those predicted by simulations, as seen in Fig. 6.

Clearly, the *"targeted"* sample has a large scatter in F values at high redshifts. Some of that scatter is due to projection effects, which we discuss latter. Heavy clusters of the *"targeted"* sample appear more compatible with the β-model at lower β values than the lower-mass clusters of the *"blind"* sample. At the OCRA beam separation, the low-mass clusters in both samples show very weak effects of biasing ($F \approx 1$) at the highest redshifts. On the other hand heavy halos require large corrections, some of which do not result from simple projection effects. In the next section, a selection of halos are investigated individually.

D. Analysis of individual clusters

In Fig. 6 some of the halos are selected by rectangles in the $z - F$ diagram. The properties of some of these halos are given in Table. II. Fig. 6 shows that only the lightest halos in our samples are found to be strong outliers, which is unsurprising.

We visually inspected all the clusters listed in Table II and verified that each of the clusters from rectangle "1" (halo IDs from 1 to 9, and 13) lie at sky positions that are partially within another cluster's atmosphere and also within the angular distance of the reference beam. An example of such overlap is shown in Fig. 7 (top panels).

Inspection of the three highest mass clusters in the *"targeted"* sample (halo IDs 10, 11, and 12; black dots in right panel of Fig. 6) show that two of them (IDs 11 and 12) are also affected to some degree by a LOS projection, but the morphology of halo 10 shows no signs of another halo in the composite high-resolution map. Instead, the SZ signature has a disturbed morphology with angular extents larger than a single OCRA beam separation even though all three are at redshift $z > 0.1$. This results in small F values, and motivates measurements at larger angular separations.

In order to test whether high redshift clusters that significantly contribute to the scatter in the F–z plane (Fig. 6) could also benefit from observations out to angular distances beyond $s_{\rm OCRA}$, we investigate the three most massive clusters from rectangle "2" (Fig. 6, IDs: 14,15 and 16). Their corresponding F values (Tab. II) do not seem to result from projection effects. Instead, these clusters have extended atmospheres and/or strongly disturbed and asymmetric SZ profiles (e.g. cluster 14, Fig. 8).

Some of the heavy clusters have surface brightness profiles (Fig. 8) that are strongly inconsistent with an axially-symmetric β-profile. This necessitates using more sophisticated two-dimensional profiles at the data analysis stage (Lancaster et al. 2011; Mirakhor & Birkinshaw 2016). Clearly, heavy halos generate low F values and require large flux density corrections with an OCRA type standard observational strategy (Sec. II). These low F values may partially stem from spurious projection effects (e.g. halos 11 and 12) which arise at the FOV generation stage for halos from the *"targeted"* sample (see Sec. V).

The outlying halos (rectangle "1") are either mergers (close pairs of SZ-strong halos), or have elongated of disturbed morphology (e.g. halos 3 and 4), or have small scale sub-structures. However, in many cases these properties occur at spatial scales that will not be resolved in OCRA SZ observations and/or may be relevant only as galaxy scale SZ effects that are too faint to be detected.

E. Practical aspects of using CMB templates

By subtracting the templated version of the CMB map (Sec. III B) from the pure CMB simulation, it is easy to estimate the upper limit of the residual CMB signal captured in the OCRA difference beam observations. The *Planck* 217 GHz and NILC maps have enough pixels to create a template of resolution of the order of an arcminute, and at least the former should contain only a negligible tSZ signal.

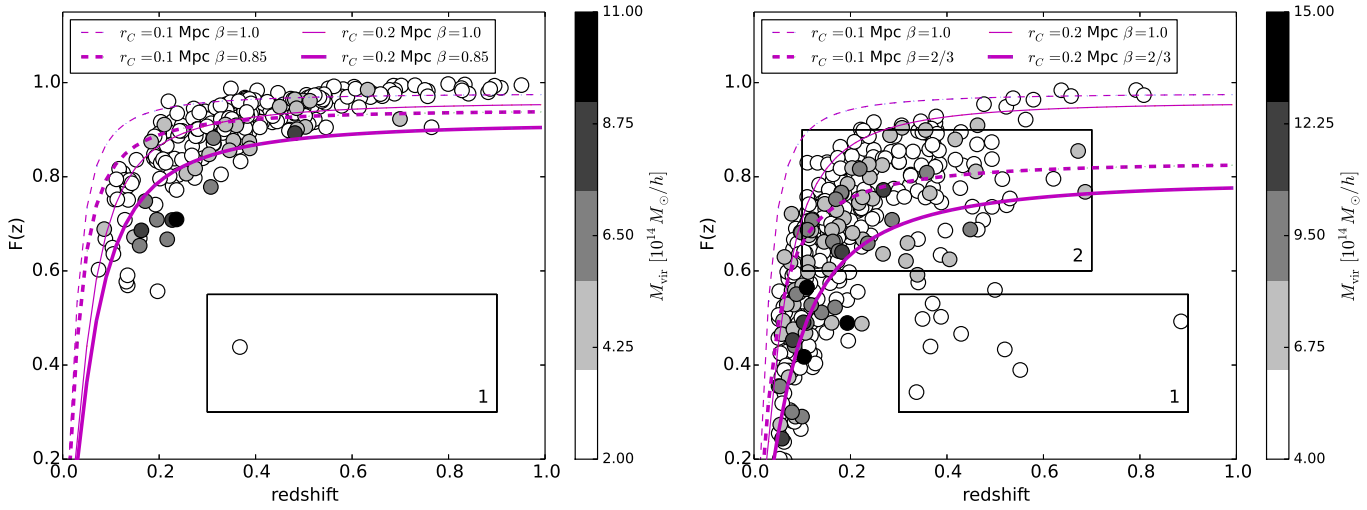

Figure 6: Simulated fractions (F) as a function of redshift and virial mass for clusters from *"blind"* (left) and *"targeted"* (right) samples and for observations at effective beams angular separation $s = 0.0526^\circ$ (the separation of OCRA beams). The fractions were measured from maps containing tSZ signal only. The lines trace the dependence for a halo described by a β-model according to Eq. 2 with parameters given in the plot legend. The rectangles "1" and "2" mark strong outliers and some halos from the main group that are inspected individually (see text for discussion).

Although subtracting CMB templates from the pure CMB maps decreases the large-scale variance by an order of magnitude, the residual variance in the map is carried by high frequency noise that will generate a small amount of dispersion in difference observations (Fig. 1 bottom-right panel). However, the residual small-scale noise should approximately average out under rotation of the beams in the sky, and since the large-scale power is effectively removed, increasing the effective separation should not suffer from exponential variance growth due to primordial CMB at arcminute angular scales.

How reliable are the 217 GHz or NILC *Planck* templates in correcting single frequency SZ observations for confusion with the primordial CMB? The 217 GHz map is foreground contaminated and the NILC map, although foreground cleaned, still may contain residual tSZ signals at scales least optimized in the needlet space.

In order to quantify the foregrounds and residual tSZ contaminaiton in each map, we calculate histograms of the temperature fluctuation distribution outside of a mask that removes the full sky except for the directions towards *Planck*-detected galaxy clusters from the PCSS SZ union R.2.08 catalog (Planck Collaboration et al. 2016d). Each non-masked region is a circular patch of radius $a = \{2.5', 5', 10', 15'\}$. Foregrounds will generate strong positive skewness in the temperature distribution, while the presence of residual tSZ in the NILC map should manifest itself by either a positive or negative skew depending on the frequency weights in the internal linear combination.

While the results of the test for the *Planck* NILC map (Fig. 9) do not give strong deviations from Gaussian simulations, the 217 GHz map generally does. The data are inconsistent with Gaussian simulations even at high galactic latitudes (Fig. 10), although the significance of the foregrounds seems to depend on the size of the circular patch. This implies that the 217 GHz frequency map cannot readily be used to mitigate the confusion due to CMB in OCRA observations without further assumptions on the foregrounds' frequency dependence. However, it should be interesting to quantify the significance of the arcminute scale Galactic foregrounds at 30 GHz at high and intermediate latitudes for OCRA difference observations with small beam separations. *Planck*-LFI data might also help reduce these foregrounds, though we do not study this here.

Since the foreground cleaned NILC map is statistically consistent with Gaussian simulations (Planck Collaboration et al. 2016c,e) towards the *Planck*-detected galaxy clusters (Fig. 9), it should also be suitable for mitigating CMB confusion in OCRA observations in directions outside of the mask where clusters undetected by *Planck* lie.

F. Pointing requirements

In order to quantify the implications of telescope pointing errors on the reconstruction of Compton y-parameters, and to define pointing requirements, we introduce a pointing precision parameter ϵ_p that defines the maximal angular distance that a primary beam can have from the intended position, and then we repeat the analysis of Sec. IV A. The pointing error p is drawn from a uniform distribution on $[0, \epsilon_p]$, since the RT32 pointing and tracking are dominated by systematic errors, and we investigate different values of ϵ_p. Since galaxy cluster SZ profiles are typically steep functions of angular separation, any pointing inaccuracy will lead to biasing measurements of the central comptonization parameter when taking averages from multiple observational sequences.

Figure 11 shows that for the *"targeted"* sample, i.e. typically heavy clusters, pointing error up to $\epsilon_p \approx \mathrm{HPBW}/4$ should not lead to strong ($> 10\%$) extra biases relative to the $\epsilon_p = 0$ case.

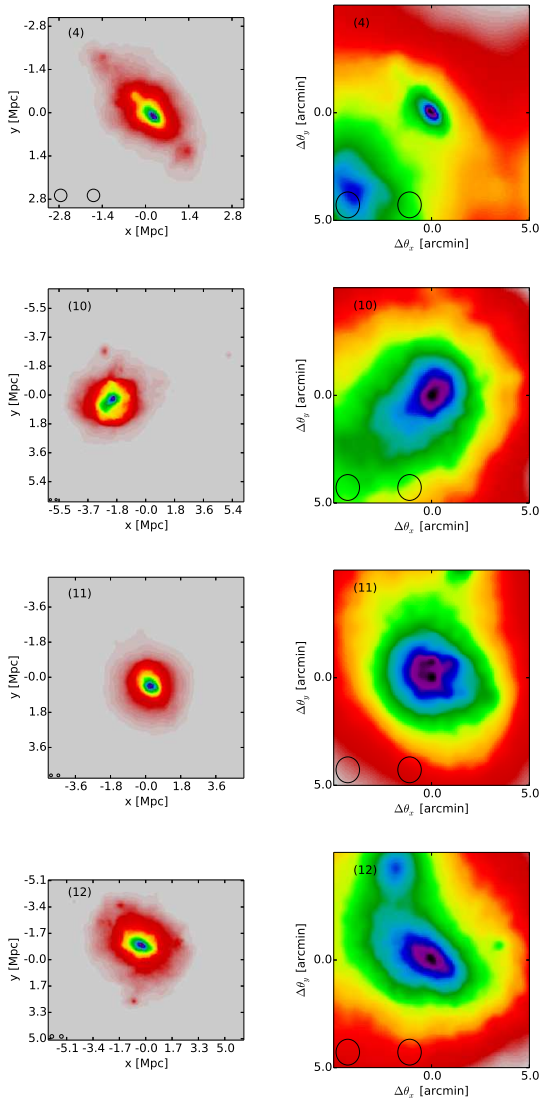

Figure 7: Selection of simulated Compton y-parameter profiles (in arbitrary units) for halos from Table. II. The panels show profiles for individual halos in physical coordinate space (*left*), and their coarse-grained version obtained from high resolution maps in angular space with contributions from other halos along the LOS (*right*). The position of halos in the left-hand side panels is defined by a box size that contains all FOF particles of the halo associated with a given cluster. In the right-hand side panels the SZ peak for the cluster is located in the plot center. For any given cluster the flux density calculation is done at the sky position of the peak. For each cluster the black circles denote OCRA FWHMs and their relative separation ($s_{\rm OCRA}$).

Measurements of the *"blind"* sample, i.e. typically less massive clusters, are more sensitive to pointing errors, but if the pointing accuracy is better than $\epsilon_p = 0.005^\circ$ ($\theta_{\rm b}^{\rm OCRA} \approx 1.2'$) the additional systematic effects will be smaller than 10%. However, larger pointing errors should be taken into account at the data analysis stage. An observational campaign is currently under way to improve RT32 pointing accuracy.

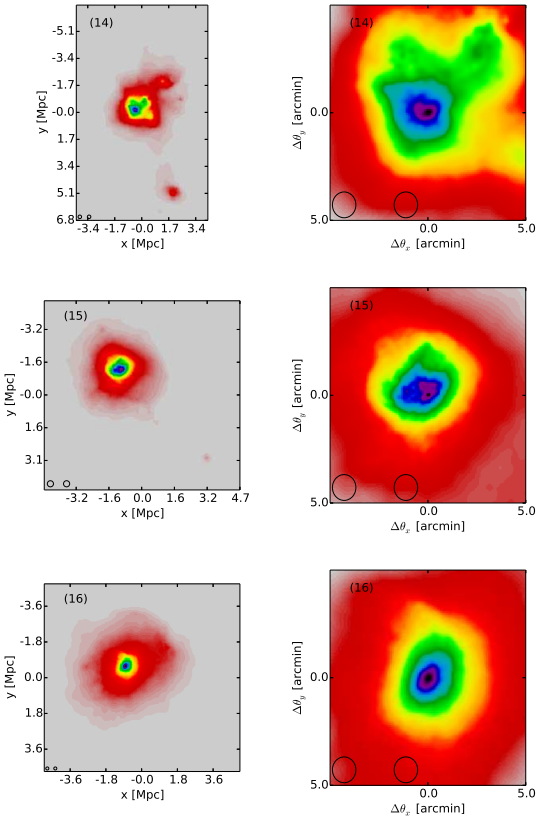

Figure 8: As in Fig. 7 but for the selection of halos from rectangle "2". See Table. II for details.

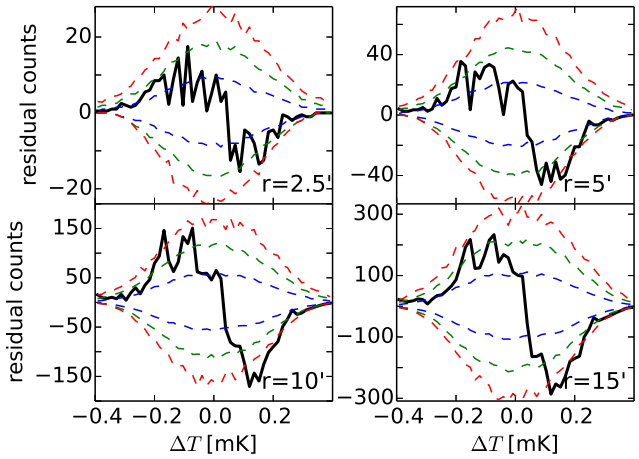

Figure 9: Residual histogram (i.e. observational pixel frequencies minus median pixel frequencies estimated from an ensemble of Gaussian NILC map simulations) of the CMB temperature fluctuations at and around the *Planck* SZ galaxy clusters, measured in the *Planck* NILC inside circular apertures of radius r centered at the clusters' positions (solid); and 1σ, 2σ and 3σ confidence contours of the pixel frequencies in these simulations (dashed).

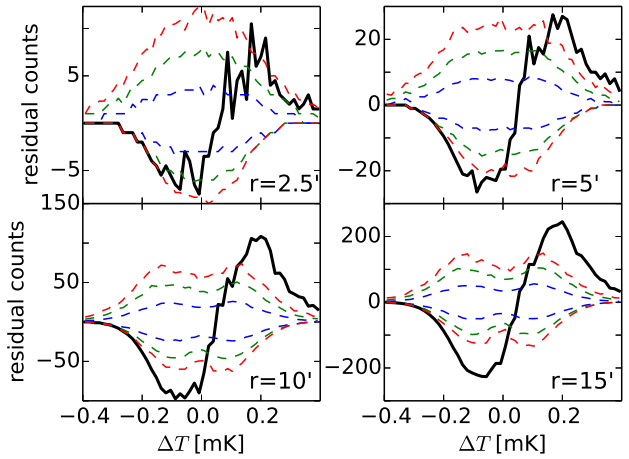

Figure 10: As in Fig. 9 but for the *Planck* 217 GHz frequency map and only for clusters at galactic latitude $b > 60^\circ$.

V. DISCUSSION

The map-making procedure that has been tested for recovering the source intensity distribution from OCRA difference measurements ($s = s_{\rm OCRA}$) assumes a flat background. This is not a problem for reconstructions of comptonization parameters from SZ observations of heavy clusters, as with the standard OCRA beam-pair separation the corrections due to CMB background are small. However, reconstructing cluster SZ profiles out to larger angular distances could benefit from correcting the difference measurements according to the *Planck* CMB template. For example, Fig. 4 (left panel) shows that an observation at $s = 2s_{\rm OCRA}$ decreases bias by $\Delta F \approx 0.2$. At the same time CMB confusion broadens the 68% CR by $\Delta F \approx 0.1$, but applying a *Planck* CMB template reverses this effect almost down to the intrinsic tSZ+kSZ scatter.

As discussed in Sec. III C the *"blind"* and *"targeted"* samples represent quite opposite observational approaches. However, since halos of the *"targeted"* sample were selected from full simulation volumes (rather than from light-cone sections), mock maps for this sample contain clusters with angular sizes calculated according to their redshifts and physical extents, as in the case of FOV simulations, but are placed in the map at rectilinearly projected locations. This contaminates the resulting maps with halos that would not fall into the assumed FOV in the standard light-cone approach. These spurious halo–halo overlaps may somewhat enlarge the 68% CR contours of various F distributions (e.g. x=tSZ or x=tSZ+CMB). A possible modification of the calculation scheme for the *"targeted"* sample would be to consider each halo independently, thus completely ignoring the intrinsic projection effects that exist in the light-cone approach, or by extending the FOV to a hemisphere (which would probably require implementing adaptive resolution maps to maintain the angular resolution of the present calculations).

The cluster samples that we analyze were not screened to select virialized clusters. Although we analyzed sub-samples selected using a virialization criterion (based on ratios of potential to kinetic energy of FOF halo particles) the results presented here are based on the full sample in order to retain a morphological variety of SZ galaxy cluster profiles (Figs. 7 and 8), and to expose the complexity of SZ flux density reconstructions from observations that do not intend to create multi-pixel intensity maps.

VI. CONCLUSIONS

We quantify the significance of systematic effects arising in dual-beam, differential observations of Sunyaev-Zel'dovich (SZ) effect in galaxy clusters. We primarily focus on effects relevant to the reconstruction of comptonization parameters from single frequency flux-density observations performed with the One Centimeter Receiver Array (OCRA) – a focal plane receiver with arcminute scale beamwidths and arcminute scale beam separations – installed on the 32 m radio telescope in Toruń.

Using numerical simulations of large scale structure formation we generate mock cluster samples (i) from blind surveys in small fields of view and (ii) from volume limited targeted observations of the most massive clusters (Sec. III C). Using mock intensity maps of SZ effects we compare the true and recovered SZ flux densities and quantify systematic effects caused by the small beam separation, by primary CMB confusion and by telescope pointing accuracy.

We find that for massive clusters the primary CMB confusion does not significantly affect the recovered SZ effect flux density with OCRA beam angular separation of $\approx 3'$. However, these observations require large corrections due to the differential observing strategy. On the other hand, measurements of SZ-faint (or high redshift $0.4 < z < 1.0$) clusters may have their SZ photometry erroneously estimated by 10% or more due to CMB confusion, which becomes stronger in observations that map larger angular distances from cluster centers.

We investigate the possibility of mitigating the CMB confusion in SZ observations that map scales beyond $3'$ from cluster centers by using *Planck* CMB 217 GHz and foreground reduced NILC maps as primary CMB templates. Using simulations we find that these templates have sufficiently high angular resolution/low noise to significantly mitigate CMB confusion in 30 GHz observations of high-z clusters, given that the templates do not contain residual foregrounds. Using a simple one-point statistic, targeted towards directions of known clusters, we verify that at least the *Planck* NILC map should also be sufficiently free from foregrounds to serve as a primary CMB template (Sec. IV E) that could improve OCRA-SZ or similar observations extended to larger angular scales (Sec. II).

Finally, we find that RT32 telescope pointing and tracking accuracy $\epsilon_p < 0.005^\circ$ should keep systematic errors in recovered SZ flux densities (comptonization parameters) below $\approx 5\%$ (after correcting for other systematic effects) even in observations of SZ-weak clusters (Sec. IV F).

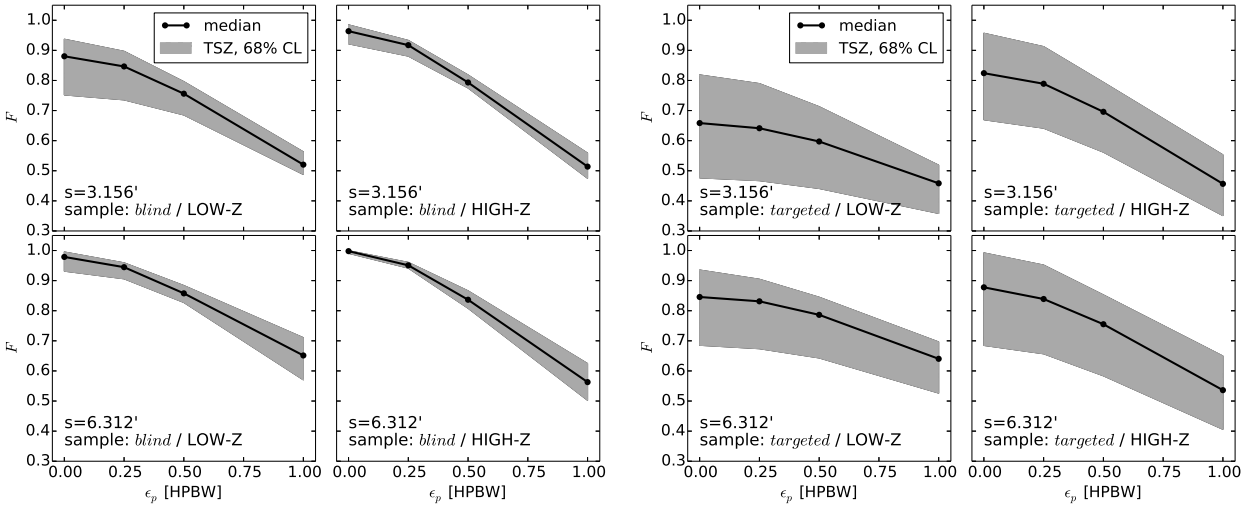

Figure 11: Systematic effects in tSZ flux density reconstruction from dual-beam observations as a function of telescope pointing errors (ϵ_p) and beam separation s for the *"blind"* sample (left) and for the *"targeted"* sample (right). The reference beam is assumed to cover all possible parallactic angles for any given galaxy cluster.

Acknowledgments

Thank you to Mark Birkinshaw for discussion on OCRA observational strategies, and to an anonymous referee for useful comments. This research has made use of a modified version of the GPL-licensed ccSHT library. We also acknowledge use of the matplotlib plotting library (Hunter 2007). This work was financially supported by the Polish National Science Centre through grant DEC-2011/03/D/ST9/03373. A part of this project has made use of computations made under grant 197 of the Poznań Supercomputing and Networking Center (PSNC).

Adam, R., Comis, B., Macías-Pérez, J. F., et al. 2014, A&A, 569, A66, [arXiv:1310.6237]
Bender, A. N., Kennedy, J., Ade, P. A. R., et al. 2016, MNRAS, 460, 3432
Birkinshaw, M. & Lancaster, K. 2005, in Background Microwave Radiation and Intracluster Cosmology, ed. F. Melchiorri & Y. Rephaeli, Vol. 2005937974, 127
Bleem, L. E., Stalder, B., de Haan, T., et al. 2015, ApJS, 216, 27, [arXiv:1409.0850]
Browne, I. W., Mao, S., Wilkinson, P. N., et al. 2000, in Society of Photo-Optical Instrumentation Engineers (SPIE) Conference Series, Vol. 4015, Radio Telescopes, ed. H. R. Butcher, 299–307
Calvo, M., Benoît, A., Catalano, A., et al. 2016, Journal of Low Temperature Physics, 184, 816, [arXiv:1601.02774]
Dawson, K. S., Holzapfel, W. L., Carlstrom, J. E., Joy, M., & LaRoque, S. J. 2006, ApJ, 647, 13, [arXiv:astro-ph/0602413]
Delabrouille, J., Cardoso, J.-F., Le Jeune, M., et al. 2009, A&A, 493, 835, [arXiv:0807.0773]
Dobbs, M., Halverson, N. W., Ade, P. A. R., et al. 2006, New A Rev., 50, 960
Górski, K. M., Hivon, E., Banday, A. J., et al. 2005, ApJ, 622, 759, [arXiv:astro-ph/0409513]
Hasselfield, M., Hilton, M., Marriage, T. A., et al. 2013, J. Cosmology Astropart. Phys., 7, 8, [arXiv:1301.0816]
Hunter, J. D. 2007, Computing In Science & Engineering, 9, 90
Lancaster, K., Birkinshaw, M., Gawroński, M. P., et al. 2011, MNRAS, 418, 1441, [arXiv:1106.3766]
Lancaster, K., Birkinshaw, M., Gawroński, M. P., et al. 2007, MNRAS, 378, 673, [arXiv:0705.3336]
Lew, B., Birkinshaw, M., Wilkinson, P., & Kus, A. 2015, J. Cosmology Astropart. Phys., 2, 4, [arXiv:1410.3660]
Lew, B. & Uscka-Kowalkowska, J. 2016, MNRAS, 455, 2901, [arXiv:1506.00225]
Lewis, A., Challinor, A., & Lasenby, A. 2000, ApJ, 538, 473, [arXiv:astro-ph/9911177]
Lin, K.-Y., Nishioka, H., Wang, F.-C., et al. 2016, ArXiv e-prints, [arXiv:1605.09261]
Mantz, A. B., Abdulla, Z., Carlstrom, J. E., et al. 2014, ApJ, 794, 157, [arXiv:1401.2087]
Melin, J.-B., Bartlett, J. G., & Delabrouille, J. 2006, A&A, 459, 341, [arXiv:astro-ph/0602424]
Mirakhor, M. S. & Birkinshaw, M. 2016, MNRAS, 457, 2918, [arXiv:1601.05304]
Muchovej, S., Leitch, E., Culverhouse, T., Carpenter, J., & Sievers, J. 2012, ApJ, 749, 46, [arXiv:1202.0527]
Peel, M. 2010, PhD thesis, ArXiv e-prints, [arXiv:1006.2760]
Peel, M. W., Gawroński, M. P., Battye, R. A., et al. 2011, MNRAS, 410, 2690, [arXiv:1007.5242]
Planck Collaboration, Adam, R., Ade, P. A. R., et al. 2016a, A&A, 594, A9, [arXiv:1502.05956]
Planck Collaboration, Adam, R., Ade, P. A. R., et al. 2016b, A&A, 594, A8, [arXiv:1502.01587]
Planck Collaboration, Ade, P. A. R., Aghanim, N., et al. 2016c, A&A, 594, A16, [arXiv:1506.07135]
Planck Collaboration, Ade, P. A. R., Aghanim, N., et al. 2016d, A&A, 594, A26, [arXiv:1507.02058]

Planck Collaboration, Ade, P. A. R., Aghanim, N., et al. 2016e, A&A, 594, A17, [arXiv:1502.01592]
Planck Collaboration, Ade, P. A. R., Aghanim, N., et al. 2011, A&A, 536, A8, [arXiv:1101.2024]
Reichardt, C. L., Stalder, B., Bleem, L. E., et al. 2013, ApJ, 763, 127, [arXiv:1203.5775]
Rumsey, C., Olamaie, M., Perrott, Y. C., et al. 2016, MNRAS, 460, 569, [arXiv:1604.06120]
Sunyaev, R. A. & Zeldovich, Y. B. 1970, Ap&SS, 7, 3
Vikhlinin, A., Kravtsov, A., Forman, W., et al. 2006, ApJ, 640, 691, [arXiv:astro-ph/0507092]
Zwart, J. T. L., Barker, R. W., Biddulph, P., et al. 2008, MNRAS, 391, 1545, [arXiv:0807.2469]